nature communications

Article

https://doi.org/10.1038/s41467-026-79335-6

Machine learning-driven regulation of the four-electron LiOH pathway in lithium–oxygen batteries with prolonged cycling

Received: 19 February 2026

Accepted: 14 October 2026

Published online: 18 November 2026

Check for updates

Tiansheng Bai[1,7], Yiming Hu[1,7], Wei Zhai[2,7], Xiongwei Zhong[3,7], Jinru Huang[1], Jiaxian Wang[1], Wei Song[1], Teng Rao[1], Shengchuang Du[4], Dandan Gao[5] ✉, Jingyu Lu[4] ✉, Rongpei Shi[1] ✉, Lijie Ci[1,6] ✉ & Deping Li[1,6] ✉

The practical deployment of high-energy-density lithium–oxygen batteries is fundamentally restricted by sluggish oxygen redox kinetics and the instability of discharge intermediates. Here, we report an artificial intelligence-integrated framework leveraging interpretable machine learning and density functional theory to navigate a vast chemical space of thousands of active sites. This approach identifies Ni-Co dual-atom catalysts as a better configuration among the selected elements for orchestrating multi-electron transfer. Theoretical analysis reveals that synergistic electronic coupling between the dual-sites fundamentally reconfigures the *d*-band center, thereby lowering the thermodynamic barriers for oxygen redox. Moreover, the catalysts enable precise regulation of the reaction pathway, inducing a controllable transition from the conventional two-electron pathway to a four-electron pathway. This shift yields a discharge capacity of ~60,000 mAh g^{-1}. Beyond its role as a positive electrode catalyst, this architecture functions as a multifunctional interfacial protective layer that stabilizes the lithium metal negative electrode by suppressing dendrite growth. Consequently, the lithium–oxygen system achieves stable lifespan of 2075 cycles under the four-electron pathway with reduced voltage decay. This work establishes a data-guided strategy for the rational design of atomic-scale architecture via artificial intelligence, unlocking the potential of multi-electron oxygen chemistry for lithium–oxygen batteries.

The pursuit of energy storage systems with energy densities comparable to gasoline has positioned lithium–oxygen (Li-O_2) batteries, which have a high theoretical specific energy of ca. 3500 Wh kg^{-1} (based on the combined mass of Li and O_2 consumed to form Li_2O_2 during discharge), as a candidate technology for future electrification[1–4]. However, their practical viability is fundamentally constrained by the conventional two-electron ($2e^-/O_2$) transfer pathway ($2Li + O_2 + 2e^- \leftrightarrow Li_2O_2$), which produces insulating and insoluble lithium peroxide. This reaction product inevitably passivates the positive electrode interface,

A full list of affiliations appears at the end of the paper. ✉e-mail: dandan.gao@uni-mainz.de; lujingyu@hit.edu.cn; shirongpei@hit.edu.cn; cilijie@hit.edu.cn; lideping@hit.edu.cn

leading to sluggish redox kinetics, severe overpotentials, and poor cycle life (Fig. 1a)[5,6].

To overcome the thermodynamic and kinetic limitations of Li_2O_2-based reaction pathway, shifting the reaction trajectory toward a four-electron ($4e^-/O_2$) pathway to form lithium hydroxide (LiOH) has emerged as a promising strategy[7,8]. The LiOH chemistry not only offers better chemical stability and higher theoretical capacity but also mitigates the severe pore clogging associated with Li_2O_2[9,10]. However, engineering such a precise pathway transition requires a catalyst surface capable of delicately balancing the adsorption of protonated intermediates. Unfortunately, this requirement is often fundamentally restricted by the linear scaling relations inherent to traditional single-metal active sites[11–15].

Breaking these catalytic bottlenecks requires expanding the design space from single atoms to multi-metallic configurations, where synergistic electronic coupling can decouple adsorption energies. Dual-atom catalysts (DACs) provide a highly tunable platform where synergistic electronic coupling can reconfigure local d-band centers, thereby optimizing the kinetics of proton-coupled electron transfer (PCET). However, the combinatorial complexity of dual-metal pairs and coordination environments renders traditional trial-and-error exploration inefficient and costly. In this context, machine learning (ML) has emerged as an essential tool for accelerating materials discovery[16–18]. The combinatorial complexity arising from diverse metal pairings and coordination environments renders exhaustive experimental screening intractable[19]. By elucidating the high-dimensional, non-linear correlations linking intrinsic physicochemical descriptors such as electronegativity and valence electron configuration to electrochemical performance, data-driven protocols can efficiently navigate the vast chemical space to identify better heteronuclear active sites that elude conventional heuristic intuition.

Herein, we establish an integrated artificial intelligence (AI) framework that leverages interpretable machine learning alongside density functional theory (DFT) to guide the rational design of dual-atom catalysts for high-performance Li–O_2 batteries. Guided by the critical descriptors extracted from our analysis, the ML model pinpointed the Co–Ni dual-site configuration as a better architecture for regulating oxygen redox pathways. Theoretical validation confirms that the electronic synergy between Ni and Co atoms reconfigures the local d-band structure, effectively lowering the thermodynamic barriers for the four-electron LiOH pathway. Experimentally, the synthesized NiCo-DACs enable a controllable transition from Li_2O_2 to LiOH formation, delivering a substantial capacity of ca. 60,000 mA h g^{-1} while sustaining over 2000 stable cycles. Furthermore, we demonstrate that this dual-atom architecture functions as a bifunctional stabilizer, simultaneously catalyzing positive electrode reactions and protecting the lithium metal negative electrode from dendrite growth. This work establishes a promising methodology for the AI-guided design of multi-electron electrochemistry, bridging the gap between atomic-scale theory and practical energy storage applications.

Results

Data-driven discovery and electronic validation of Co–Ni dual-sites

To systematically explore the catalytic design space, we focused on multi-site configurations composed of transition and noble metals (e.g., Mn, Fe, Co, Ni, Ru, and Pt) coordinated with non-metallic elements to form M–N_x active centers (Fig. 1b). A comprehensive database was constructed to trace the catalytic origin, incorporating thousands of data points characterized by nearly 50 multidimensional features across atomic, electronic, and physical descriptors (Fig. 1c and Table S1). Preliminary analysis indicated that most individual features exhibit no clear linear correlation with overpotential (Y_1), highlighting the high-dimensional complexity of the catalytic origin and the necessity of employing robust ML models to capture intricate intrinsic relationships (Figs. S1–S5). To address this, we trained eight distinct regression models, including four non-linear methods (Random Forest, ExtraTrees, GradientBoosting, and XGBoost) and four linear methods (LASSO, Ridge, SVM, and ElasticNet). Each model underwent rigorous gridded hyperparameter optimization and five group-wise folds to ensure maximum predictive accuracy and robustness (Fig. S6). Based on the R_{test}^2 coefficient, XGBoost was identified as a better model ($R^2 = 0.8815 \pm 0.0346$ on the test set, Fig. 1d). In addition, we also conducted 50 held-out folds in total with 10 random seeds on this model to avoid the randomness of this result, and it showed that the average R^2 of different random seeds was not less than 0.85, ensuring robust stability and predictive performance (Fig. 1f–h).

To elucidate the physical basis of the model predictions, we conducted SHapley Additive exPlanations (SHAP) feature importance analysis to extract the physicochemical descriptors governing activity (Fig. 1e and Table S2). The results indicate that intrinsic electronic properties are the dominant factors, particularly the correlation of d electron number of the main metal site (M_1) with the electronegativity of the non-metal site (N), the correlation of d-band electron number of M_1 with the average electronegativity of the second metal site (M_2) and N, as well as the d-band center of M_1. Subsequently, we used the trained model to predict overpotential (Y_1) for different combinations of 28 candidate elements, and determined that the Co–Ni heteronuclear pair exhibited a lower overpotential. Meanwhile, it is noteworthy that, the cycling performance (Y_2, final indicators of Li-O_2 batteries) will increase with the decrease of overpotential, identifying the Co–Ni heteronuclear pair as a better configuration (Fig. 2a–d). These results are consistent with experimental observations concerning the stability of specific metal combinations (Fig. S7) and indicate that the interaction between Co and Ni atoms provides a feasible strategy to exceed the performance limits of single-site catalysts.

To substantiate the machine learning predictions with a physical basis, we conducted density functional theory (DFT) calculations to investigate the electronic structure of the identified Co–Ni dual-site configuration. The projected density of states (PDOS) analysis suggests that the electronic interaction within the Ni–Co heterostructure induces a significant reconfiguration of the d-band centers (E_d). Specifically, as shown in Fig. 2e–h, the E_d values for the NiCo-DACs system shift to a moderate energy level of approximately −2.50 eV to −2.40 eV, positioning them between the values for single-atom Co-N/rGO (−1.53 eV) and Ni-N/rGO (−2.90 eV). This intermediate orbital positioning aligns with the Sabatier principle, contributing that the adsorption strength of oxygen-containing intermediates is balanced to facilitate both efficient formation and decomposition processes[20].

Quantitative analysis of the electron density below the Fermi level further elucidates this modulation (Fig. 2i). The calculation shows a marked charge enrichment at the Co site within the dual-atom structure, reaching 8.03 |e| compared to 6.76 |e| in the single-atom counterpart, while the Ni site remains relatively stable. This localized electronic enhancement is driven by spontaneous inter-site charge transfer, which strengthens the binding interaction between active sites and oxygen-containing intermediates, thereby driving the boosted catalytic activity observed in the dual-atom configuration. Furthermore, the O 2*p* PDOS indicates that the oxygen orbitals maintain a broader distribution on the NiCo-DACs surface across various reaction intermediates (Figs. S8–S11), including O_2*, LiO_2*, Li_2O_2*, and Li_4O_4*. Such orbital broadening signifies enhanced hybridization between the oxygen species and the dual-atom substrate,

https://doi.org/10.1038/s41467-026-79335-6

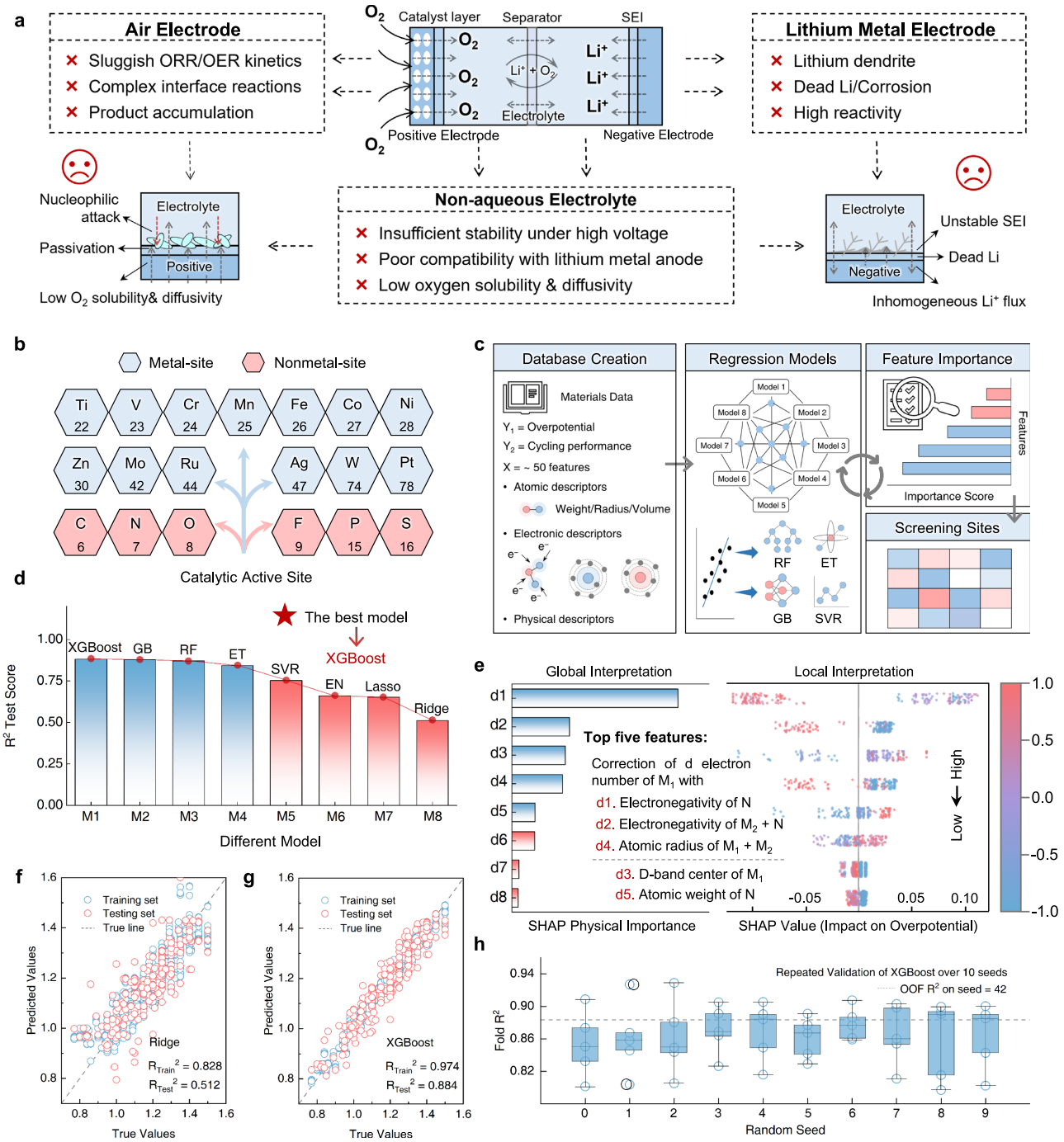

Fig. 1 | Investigation of multi-site catalyst design principle by machine learning. a Overall illustration of Li–O_2 battery, including the cell structure, reaction mechanism, and critical bottlenecks. (ORR: oxygen reduction reaction; OER: oxygen evolution reaction; SEI: solid electrolyte interphase). **b** The commonly used catalytic elements in current lithium oxygen batteries include both metallic and non-metallic sites. **c** Overall workflow diagram of used machine learning. Four major parts: initial data set construction (Y_1: overpotential; Y_2: cycling performance), eight regression models training (such as RF: Random Forest; ET: Extremely Randomized Trees; GB: Gradient Boosting; SVR: Support Vector Regression), SHAP (SHapley Additive exPlanations) feature importance analyzing, and catalytic elements screening for performance prediction through above trained model. **d** Comparison of the eight regression models (XGBoost: eXtreme Gradient Boosting; GB: Gradient Boosting; ET: Extremely Randomized Trees; SVR: Support Vector Regression; EN: Elastic Net; Lasso: Least Absolute Shrinkage and Selection Operator; M1–M8, the above eight machine-learning models) based on the coefficient of determination (R^2) calculated for five held-out group-wise folds. The reported values are the mean ± standard deviation across the five folds ($(n = 5)$ fold-level evaluations per model). Groups were defined by the literature-source identifier, with the primary five-fold assignment generated using random seed 42. XGBoost showed the highest predictive performance, with ($R^2 = 0.8815 \pm 0.0346$). **e** SHAP summary: feature importance analysis of the XGBoost model on overpotential. Cross-validated parity plots for the **f** Ridge and **g** XGBoost models, respectively. Blue points represent predictions for records used to fit each fold, and red points represent predictions for the corresponding held-out records. The reported R^2 values are calculated from the pooled held-out predictions under the primary five-fold group-wise split. The search spaces and selected hyperparameters for all models are summarized in Table S7. **h** Repeated group-wise validation of the optimized XGBoost model using 10 random grouping seeds. Each seed generated five group-wise folds, yielding 50 fold-level evaluations in total. Each point represents the (R^2) of one held-out fold ($(n = 5)$ per seed); the center line of each box denotes the median, the box spans the 25th–75th percentiles, and the whiskers extend to the most extreme values within 1.5 times the interquartile range. The random seed 42 denotes the primary fold assignment.

https://doi.org/10.1038/s41467-026-79335-6

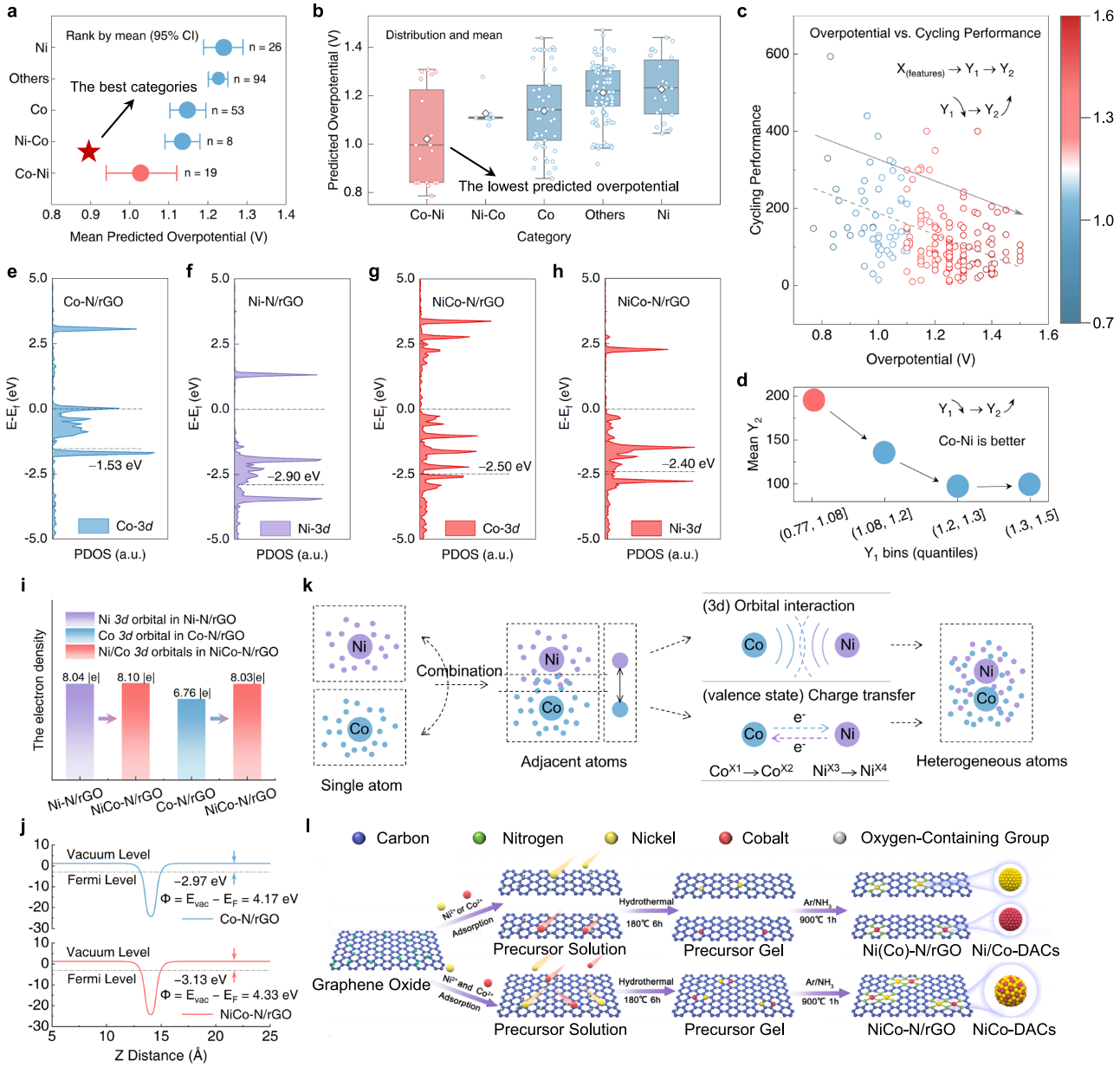

Fig. 2 | Catalytic elements screening results and DFT pre-analysis for feasibility. Analysis of overpotential prediction values for different elements of **a** mean predicted overpotential for each catalyst category. The filled circle indicates the arithmetic mean predicted overpotential, and the horizontal error bar indicates the 95% confidence interval calculated as $x \pm 1.96 \times SD/\sqrt{(n)}$. Here, n denotes the number of catalyst records in each category: Co–Ni ($n = 19$); Ni–Co ($n = 8$); Co ($n = 53$); Others ($n = 94$); and Ni ($n = 26$). **b** Distribution of predicted overpotentials for the same categories. The horizontal line inside each box denotes the median; the lower and upper boundaries of the box denote the 25th and 75th percentiles, respectively; and the whiskers extend to the most extreme observations within (1.5 × IQR), where (IQR = Q_3-Q_1). The white diamond denotes the arithmetic mean. Open circles represent individual catalyst records, including observations outside the whisker limits; therefore, the open circles should not be interpreted as a separate set of experimentally replicated outliers. The sample sizes are Co–Ni ($n = 19$); Ni–Co ($n = 8$); Co ($n = 53$); Others ($n = 94$); and Ni ($n = 26$). **c** The relationship between overpotential (Y_1) and cycling number (Y_2). **d** Mean cycling performance (Y_2) within different overpotential (Y_1) intervals. The projected density of states (PDOS) of the **e** Co site in Co-N/rGO, **f** Ni site in Ni-N/rGO, **g** Co site in NiCo-DACs and **h** Ni site in NiCo-DACs. **i** The electron density below the Fermi level of the Co or Ni 3*d* orbitals in Ni-N/rGO, Co-N/rGO, and NiCo-DACs. **j** Work function (Φ) profiles of Ni-N/rGO and NiCo-DACs (E_{vac}: vacuum energy level; E_F: Fermi level). Mechanism diagram **k** and schematic diagram **l** of the NiCo dual-atom catalyst. Source data are provided as a Source Data file.

effectively lowering the kinetic barriers for the formation and decomposition of subsequent discharge products[21].

Additionally, the modulation of the surface charge distribution is reflected in the work function profiles ($\Phi = E_{vac} - E_F$), where the NiCo-DACs exhibit a modified value of 4.33 eV compared to 4.17 eV for Co-N/rGO, suggesting an optimized energy barrier for electron escape from the Fermi level (Fig. 2j). These combined electronic features provide a theoretical validation for the enhanced catalytic activity of the NiCo dual-atom architecture, and the underlying catalytic mechanisms, including optimized orbital hybridization and enhanced charge transfer processes are schematically summarized in Fig. 2k.

Atomic configuration and coordination environment of NiCo-DACs

Based on these theoretical insights, we synthesized nitrogen-doped reduced graphene oxide-supported NiCo dual-atom catalysts (NiCo-

DACs) and their single-atom counterparts (Ni/Co-SACs) to evaluate the structural validity of the ML-predicted model. As depicted in Figs. 2l and S12–18, the NiCo-DACs exhibit a typical graphene-like morphology with uniformly distributed Ni, Co, and N elements, while the absence of lattice fringes in high-resolution transmission electron microscopy (HRTEM) images confirms that no metal-based nanoparticles or alloys were formed. This dispersion phenomenon is further corroborated by the X-ray diffraction (XRD) and Raman spectra (Figs. S19 and S20), where the presence of only characteristic graphitic carbon peaks and the similar D/G band intensity ratios rule out the existence of crystalline metal aggregates. To visualize the atomic configuration at the sub-nanometer scale, we employed high-resolution high-angle annular dark-field scanning transmission electron microscopy (HAADF-STEM). In contrast to the isolated metal sites observed in the SAC samples, the NiCo-DACs predominantly feature diatomic metal pairs with a statistical interatomic distance of approximately 0.33 nm (Fig. 3a–h), providing direct visual evidence of the successful construction of the targeted dual-metal architecture. Furthermore, N_2 adsorption/desorption isotherm results (Figs. S21–25) demonstrate that the DACs possess a higher specific surface area and an optimized pore size distribution, which facilitates the highly dispersed metal sites for enhanced Li^+ diffusion and restrained volume expansion during cycling.

To decipher the specific coordination environment and electronic states of these dual sites, we utilized element-selective X-ray absorption spectroscopy (XAS), as the low metal loading (<0.2 wt%) precluded detailed analysis via standard X-ray photoelectron spectroscopy (XPS, Figs. S26–28). The X-ray absorption near-edge structure (XANES) indicates that the oxidation states of both Ni and Co in $NiCo_2$-DACs and Ni/Co SACs lie between 0 and +2. Notably, a quantitative analysis of the absorption edges reveals a distinct valence shift induced by the dual-atom configuration, in which the average valence of Ni decreases from 1.12 in Ni-SACs to 0.78 in NiCo-DACs, while the Co valence increases from 1.26 to 1.32 (Fig. 3i–l). This experimental evidence of inter-site charge transfer is consistent with our DFT predictions and is further corroborated by electron localization function (ELF) simulations (Fig. 3m), which visualize a distinct depletion of electron density around Co atoms. As schematically illustrated in Fig. 3n, this redistribution confirms a spontaneous directional electron flow from the high-density donor (Co) to the lower-density acceptor (Ni), effectively modulating the electronic states of catalytic centers for optimized performance.

The local coordination environment was further deciphered through k^3-weighted Fourier transform (FT) extended X-ray absorption fine structure (EXAFS) analysis. The Co K-edge spectrum of the NiCo-DACs exhibits two distinct scattering peaks at approximately 1.2 and 2.0 Å (Fig. 3o), which correspond to Co–N coordination shells with differing orientations in the first shell. Notably, compared to Co-SACs, the intensity and position of these peaks are clearly modulated by the presence of the neighboring Ni atom (Figs. S29, S30, and Table S3). This structural evolution is visually confirmed by the wavelet transform (WT) analysis of the Co K-edge (Figs. 3p and S31). Subsequently, to further validate the evolution of the nitrogen coordination environment, high-resolution N 1*s* XPS spectra were deconvoluted into four distinct components (Figs. 3q, r, and S32), where the binding energy of the pyridinic-N species in $NiCo_{1.2}$-DACs shifts to an intermediate position between those of the Ni-SACs and Co-SACs, while the corresponding peak for $NiCo_3$-DAC gravitates toward the value of the Co-SACs. This systematic spectral shift provides evidence for the transformation from isolated M–N configurations to a heteronuclear Ni/Co–N coordination sphere, where the local electronic environment is explicitly modulated by the relative Ni/Co atomic ratio (Fig. 3s). Collectively, these findings support the proposed electronic structure and coordination geometry of the synthesized NiCo-DACs.

Reversible 4e⁻ LiOH chemistry for Li–O_2 batteries with prolonged stability

To evaluate the impact of the engineered electronic structure on electrochemical performance, we systematically investigated the catalytic activity of NiCo-DACs using galvanostatic discharge–charge measurements. In a standard anhydrous electrolyte, as profiled in Figs. 4a and S33, the NiCo-DACs electrode delivers an enhanced specific capacity of ca. 25,000 mA h g^{-1}, compared with ~17,000 mA h g^{-1} for the Ni/Co-SACs counterparts. Meanwhile, the $NiCo_2$ group exhibits the highest capacity retention of approximately 100% (calculated as $Q_{200}/Q_{100} \times 100\%$) and the lowest discharge overpotential (~0.29 V), demonstrating its better catalytic activity and structural stability. Subsequently, the intrinsic kinetic advantage of the dual-atom sites is further manifested in cyclic voltammetry (CV) tests, where the NiCo-DACs exhibit a significantly larger integrated curve area and more pronounced redox peaks compared to the baselines, alongside a positive shift in the cathodic onset potential (Fig. 4b). This enhanced catalytic efficiency is quantitatively corroborated under capacity-limited cycling (500 mA h g^{-1}), where the $NiCo_2$-DACs achieve a low charge–discharge voltage gap of only 0.83 V, which is substantially lower than those of other DACs (0.97 V/1.48 V) and SACs (1.38 V/1.51 V) (Fig. 4c). Collectively, these results demonstrate that the $NiCo_2$-DACs electrode possesses a significantly higher density of accessible active sites, which effectively lowers the kinetic barriers for electrochemical reactions. Consistent with these findings, rate capability tests demonstrate that the dual-atom catalyst maintains the lowest voltage polarization across a wide range of specific current from 100 to 800 mA g^{-1} (Fig. 4d), highlighting the enhanced catalytic efficiency of the rationally designed dual-atom architecture.

The ex situ XRD patterns of the discharged positive electrode reveal that the discharge products consist of a mixture of Li_2O_2 and LiOH (Fig. 4e). Therefore, we recognized the potential to optimize this system by steering the reaction toward the more stable proton-coupled four-electron pathway. To this end, we strategically introduced controlled amounts of H_2O (1 vol%, 3 vol%, and 5 vol%) into the electrolyte (Fig. 4f) to induce a complete transition from the 2e⁻ to the 4e⁻ reaction pathway.

This modulation induced an enhancement in performance, enabling the discharge capacity to surge to ca. 60,000 mA h g^{-1} (corresponding to approximately 3600 mA h g^{-1} based on the total GDL electrode mass and 35 mA h cm^{-2} based on the geometric electrode area) under 5 vol% H_2O conditions. This specific capacity is nearly double/quadruple that of the Co-SACs and rGO baseline catalyst, which exhibits a capacity of ca. 35,000/15,000 mA h g^{-1} (Figs. 4g and S34). Corresponding XRD patterns and SEM images confirm the exclusive transformation of discharge products from Li_2O_2 to crystalline LiOH (Figs. 4h and S35), which aligns with the schematic illustrations (Fig. 4i). Correspondingly, the initial discharge-charge profiles at 5 vol% H_2O content (Fig. 4j) reveal that the $NiCo_2$-DACs maintain a low overpotential (0.85 V), demonstrating that the designed dual-atom architecture also possesses favorable catalytic activity toward LiOH chemistry, which is of critical importance for the practical application of Li–O_2 batteries. Furthermore, we conducted kinetic isotope effect (KIE) measurements for assessing the role of proton transfer in the ORR process by comparing the ORR performance in protonic (0.1 M KOH in H_2O) and deuterated (0.1 M KOD in D_2O) electrolytes (Figs. S36 and S37), which confirms that proton transfer is the rate-determining step facilitated by the NiCo sites.

To demonstrate the enhanced durability of the four-electron pathway, the long-term cycling performance of the NiCo-DACs electrode was evaluated at a limited capacity of 500 mA h g^{-1} (Figs. 5a, b, and S38). In anhydrous electrolyte (0 vol% H_2O), the $NiCo_2$-DACs electrode exhibits low overpotentials for 177 cycles at 500 mA g^{-1} and 170 cycles at 200 mA g^{-1} without obvious voltage decay. In contrast, the Co-SACs electrode suffers from severe polarization failure after

https://doi.org/10.1038/s41467-026-79335-6

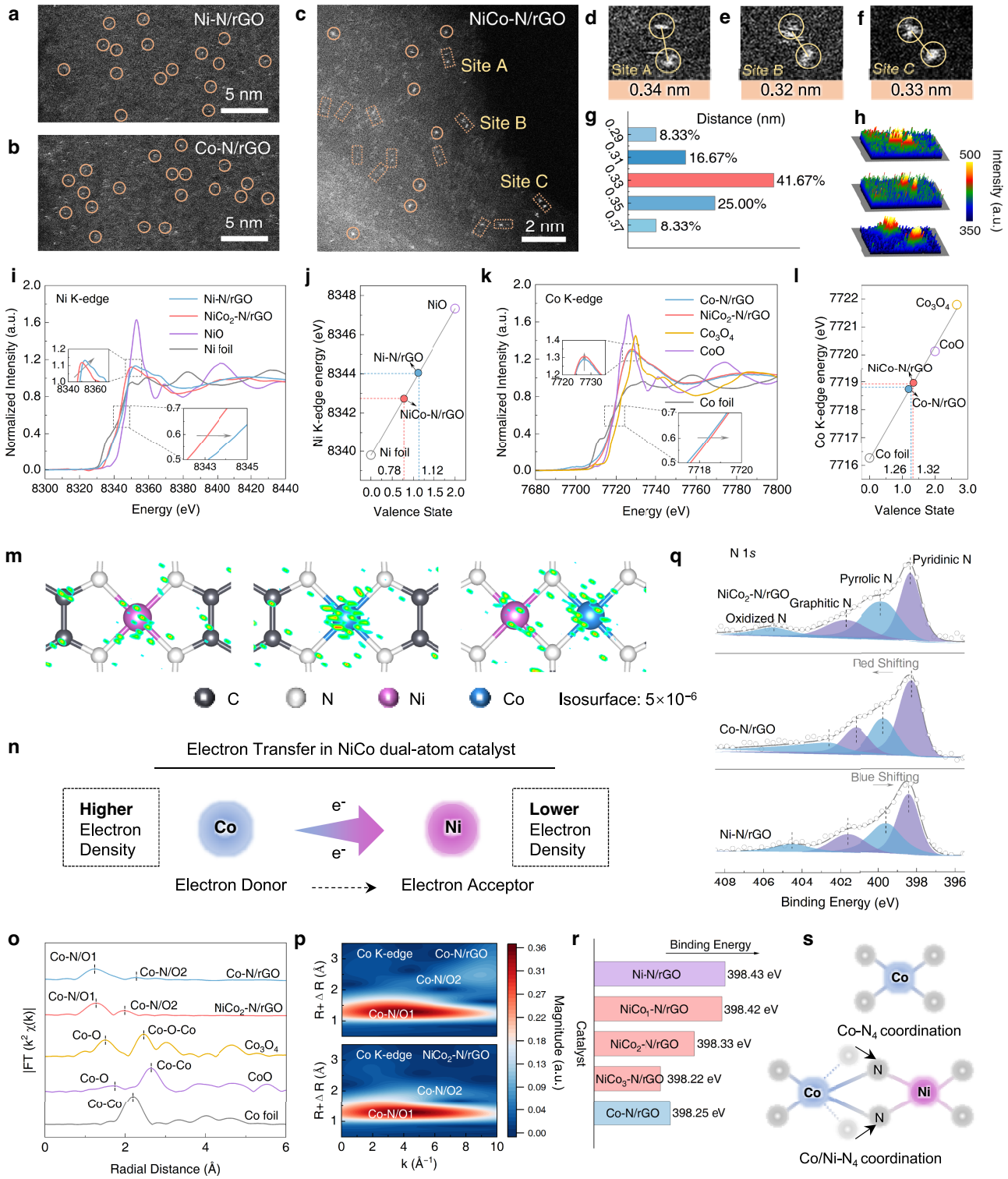

Fig. 3 | Micro-morphology and characterizations of the NiCo-DACs. High-angle annular dark-field scanning transmission electron microscopy (HAADF-STEM) images of **a** Ni-N/rGO, **b** Co-N/rGO, and **c** $NiCo_2$-N/rGO (The sites A, B, and C marked with yellow dashed lines are partially enlarged in **d**–**f**). **g** Statistical Ni–Co distance in the observed diatomic pairs ($n = 25$, each measurement represents one Ni–Co diatomic pair identified). **h** Three-dimensional morphology image of sites A, B, and C processed from HAADF-STEM images. **i**–**l** Ni and Co K-edge X-ray absorption near-edge structure (XANES) spectra, with the corresponding valence state of Ni and Co for Ni-N/rGO, Co-N/rGO, $NiCo_2$-N/rGO, and their control samples. **m** The electron localization function (ELF) plots of Ni-N/rGO, Co-N/rGO and NiCo-DACs at an isosurface level of 5×10^{-6}. The colored regions represent the positive ELF isosurface, and the same isovalue and visualization settings were used for all three structures. **n** Diagram of electronic transfer. **o** Fourier transform of Co K-edge extended X-ray absorption fine structure (EXAFS) signals for Co-N/rGO, $NiCo_2$-N/rGO and their control samples. **p** Wavelet transforms of Co K-edge EXAFS signals. **q** N 1*s* X-ray photoelectron spectroscopy (XPS) spectra of Ni-N/rGO, Co-N/rGO and $NiCo_2$-N/rGO. **r** The binding energy of pyridinic-N in different catalysts. **s** Schematic diagram of metal-nitrogen catalytic site structure. Source data are provided as a Source Data file.

https://doi.org/10.1038/s41467-026-79335-6

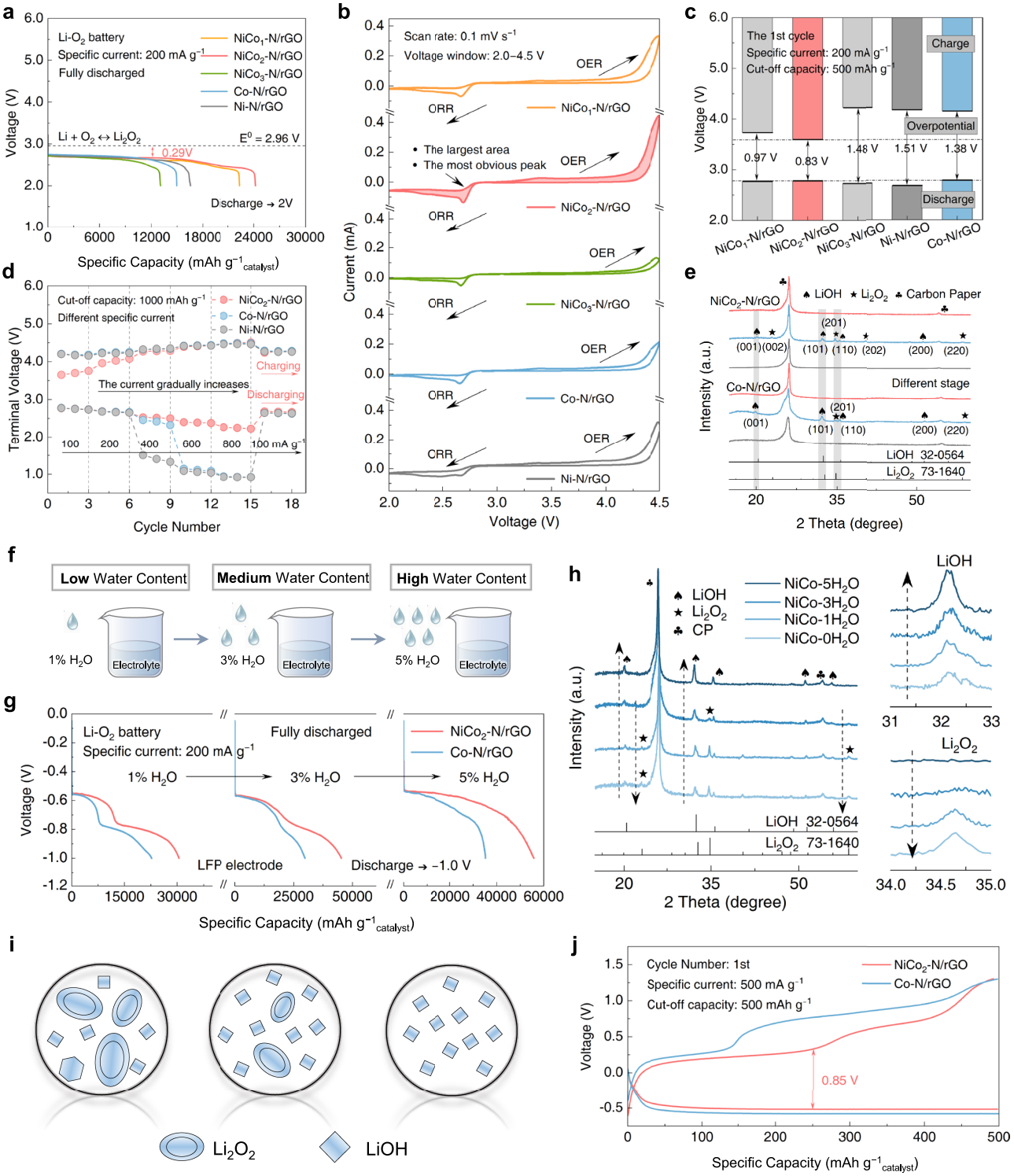

Fig. 4 | Battery performance evaluation and product control analysis. Fully discharged curves at the specific current of 200 mA g^{-1} (**a**), cyclic voltammetry (CV) curves (**b**), overpotential in the 1st cycle with a limited capacity of 500 mA h g^{-1} at the specific current of 200 mA g^{-1} (**c**), and rate performance at different specific current (**d**) for NiCo-DACs and Ni/Co-SACs electrodes. **e** X-ray diffraction (XRD) patterns for $NiCo_2$-DACs and Co-SACs electrode at the electrochemical states of pristine, fully discharged and fully charged states during the 1st cycle with a specific current 200 mA g^{-1}. The above electrochemical measurements were performed using 2032-type coin cells at 25 °C. **f** Schematic illustration of the electrolyte modulation with controlled H_2O addition. **g**, **h** Fully discharged curves at the specific current of 200 mA g^{-1} in the electrolytes with 1 vol%/3 vol%/5 vol% H_2O and corresponding XRD patterns of discharge products under 25 °C ($LiFePO_4$, (LFP) was used as the negative electrode). **i** Schematic illustration of the changes in discharge-product composition and morphology with increasing H_2O content. **j** Galvanostatic discharge-charge profiles with $NiCo_2$-DACs and Co-SACs as the positive electrode at a limited capacity of 500 mA h g^{-1} and a specific current of 500 mA g^{-1} in the electrolytes with 5 vol% H_2O. All cut-off capacities and specific currents mentioned above were normalized to the catalyst mass. Source data are provided as a Source Data file.

only 76 cycles. This trend is further elucidated by electrochemical impedance spectroscopy (EIS, Fig. S39), which reveals that the Co-SACs-based battery possesses a significantly higher charge-transfer resistance (R_{ct}). When the reaction pathway transforms from $2e^-/O_2$ to $4e^-/O_2$ in the 5 vol% H_2O electrolytes, the $NiCo_2$-DACs achieve a lifespan of 2075 cycles with reduced voltage decay, compared with the Co-SACs baseline catalyst, which suffers from rapid capacity decay and failure after only 790 cycles. Even at higher capacities and specific current (6000 mA h g^{-1}–2400 mA g^{-1}), the $NiCo_2$-DACs also demonstrate good cycling stability (Fig. S40). This favorable durability, particularly under the $4e^-$ pathway (also confirmed via characterizations under extended cycling conditions in Figs. S41–S47), substantiates the robust catalytic activity and structural integrity of the $NiCo_2$-DACs, further effectively mitigating electrolyte decomposition and parasitic side reactions, thereby extending cycle life and enhancing battery safety.

Detailed characterization of the discharge products (Fig. 5c, d) reveals that the $NiCo_2$-DACs electrode generates a higher proportion of Li_2O_2 (31.7%) than the Co-SACs (22.3%) in the anhydrous state, while both achieve a 100% conversion to LiOH in the 5 vol% H_2O added electrolyte. To unravel the reaction mechanism underpinning this reversibility, in situ differential electrochemical mass spectrometry (DEMS) was employed (Figs. 5e–g and S48). Based on the stoichiometric reactions for Li_2O_2 ($2e^-/O_2$) and LiOH ($4e^-/O_2$) formation, the calculated e^-/O_2 ratios during discharge for $NiCo_2$-DACs (3.66) and Co-SACs (3.60) confirm a hybrid $2e^-/4e^-$ process, consistent with XRD results (Fig. S49). During the charging process, the $NiCo_2$-DACs generate significantly suppressed evolution of CO_2 and CO side products compared to Co-SACs. There is no significant H_2 production during the battery operation. Moreover, the e^-/O_2 ratios of 6.71 for $NiCo_2$-DACs and 9.30 for Co-SACs during OER indicate that the dual-atom architecture substantially enhances the reversible decomposition of both Li_2O_2 and LiOH, demonstrating favorable OER catalytic efficiency. Furthermore, theoretical energy profiles suggest that the NiCo dual-site configuration optimizes the binding strength of key intermediates, thereby lowering the thermodynamic barriers for O_2/Li_2O_2/LiOH pathways (Fig. 5h). Finally, based on the XPS analysis of the intermediate species (Fig. S50), the comprehensive reaction mechanisms for the $NiCo_2$-DACs and Co-SACs-based Li–O_2 batteries are schematically summarized in Fig. 5i.

Bifunctional negative electrode protection and thermodynamic origins

Beyond the critical role of the catalyst at the positive electrode, the practical deployment of LiOH-based batteries faces the critical challenge of thermodynamic instability at the lithium metal negative electrode in the presence of proton sources such as trace H_2O. To address this issue, we investigated the potential of the NiCo-DACs architecture to serve as a lithiophilic interfacial layer for stabilizing the negative electrode (Fig. 6a). By integrating these dual-atom sites at both electrodes, the reconfigured Li–O_2 battery achieves stable operation for 185 cycles at a high capacity of 1000 mA h g^{-1} and a specific current of 1000 mA g^{-1}, surpassing the pure lithium-based system, which fails after only 32 cycles (Fig. 6b, c). Further validation using symmetric battery tests, Li||Cu battery tests, and electrochemical impedance test all confirms that the NiCo-DACs protective layer significantly enhances interfacial kinetics, reducing the overpotential by approximately 0.23 V compared to the bare lithium counterpart and stabilizing the negative electrode interface (Figs. 6d and S51–S55).

To visualize this stabilization effect, in situ optical microscopy was employed to monitor the deposition process. While whisker-shaped dendrites rapidly proliferated on the pure lithium surface, the NiCo-DACs-protected negative electrode remained smooth and dendrite-free (Fig. 6e). As schematically summarized in Fig. 6f, the NiCo-DACs demonstrate a distinct bifunctional synergistic mechanism by simultaneously regulating the reversible formation and decomposition of discharge products at the positive electrode while effectively inhibiting dendrite growth at the negative electrode. Consequently, this dual-atom architecture enables Li–O_2 batteries to achieve enhanced specific capacities, minimized overpotentials, appropriated adsorption energy, and prolonged cycling life, which is competitive to some recent relevant reports (Fig. 6g, h). These comprehensive advancements underscore the enhanced catalytic efficiency and structural robustness of the rationally designed dual-atom framework for high-energy-density energy storage applications.

To explore possible atomistic insights into the reaction mechanism, we calculated the Gibbs free energy profiles for the oxygen reduction and evolution reactions (ORR/OER) along both the $2e^-/O_2$ (Li_2O_2) and $4e^-/O_2$ (LiOH) pathways (Fig. 7a, b). Regarding the two-electron pathway, the process initiates with O_2 adsorption to form the LiO_2* intermediate, which subsequently evolves into Li_2O_2* and Li_4O_4* clusters. In contrast, the four-electron pathway branches after the LiO_2* stage toward the formation of LiOOH* and LiO*, yielding LiOH* as the final product (Figs. S56 and S57). In addition, no matter how the k-point mesh is selected, the adsorption energy calculations (Figs. 7c, d, and S58) both reveal that all oxygen-containing species exhibit more negative values on NiCo-DACs compared to Co-SACs, indicating a stronger interaction between the dual-atom sites and the reaction intermediates. Specifically, the enhanced adsorption of critical species, such as LiO_2* and LiOOH*, facilitates the smooth conversion of precursors into Li_2O_2* or LiOH* during discharge while accelerating their decomposition during charge. This mechanism effectively prevents the accumulation of insulating species and contributes to the prolonged cycling stability observed experimentally.

The thermodynamic overpotentials were further quantified based on the relationships $\eta_{ORR} = U_{eq} - U_{dc}$ and $\eta_{OER} = U_c - U_{eq}$ (Figs. 7e–j and S59, S60). Attributed to the optimized adsorption energies and enhanced electronic conductivity, the NiCo-DACs significantly reduce the overpotentials for the Li_2O_2* pathway (η_{ORR}/η_{OER} = 0.28 V/0.09 V) compared to Co-SACs (0.37 V/0.26 V). A similar trend of enhanced kinetics is also observed for the LiOH* pathway, where NiCo-DACs deliver lower overpotentials (0.83 V/0.55 V) than Co-SACs (0.93 V/0.80 V). Ultimately, these DFT results demonstrate that the dual-atom architecture effectively tailors the adsorption strength of oxygen species and optimizes the interfacial charge transfer, which fundamentally balances the reversible formation and decomposition of discharge products during long-term cycling. Nevertheless, the calculated energetics should be interpreted primarily as qualitative trends that support, rather than establish, the proposed mechanistic interpretation above.

Discussion

In summary, we have established an integrated data-driven framework that bridges the gap between atomic-scale theoretical design and the practical realization of high-energy-density storage systems. By decoupling the combinatorial complexity of heteronuclear active sites through interpretable machine learning, we identified the Ni–Co dual-atom configuration as a promising catalyst that transcends the linear scaling limitations of traditional single-atom candidates, guided by critical physicochemical descriptors including valence electron configuration and electronegativity differences. The experimental validation underscores the positive potential of this engineered electronic structure, where the synthesized NiCo-DACs enable a stable proton-coupled $4e^-/O_2$ reaction pathway, delivering a capacity of ca. 60,000 mA h g^{-1} and sustaining 2075 reversible cycles. Mechanistically, this performance is driven by spontaneous inter-site charge transfer that optimizes the d-band

https://doi.org/10.1038/s41467-026-79335-6

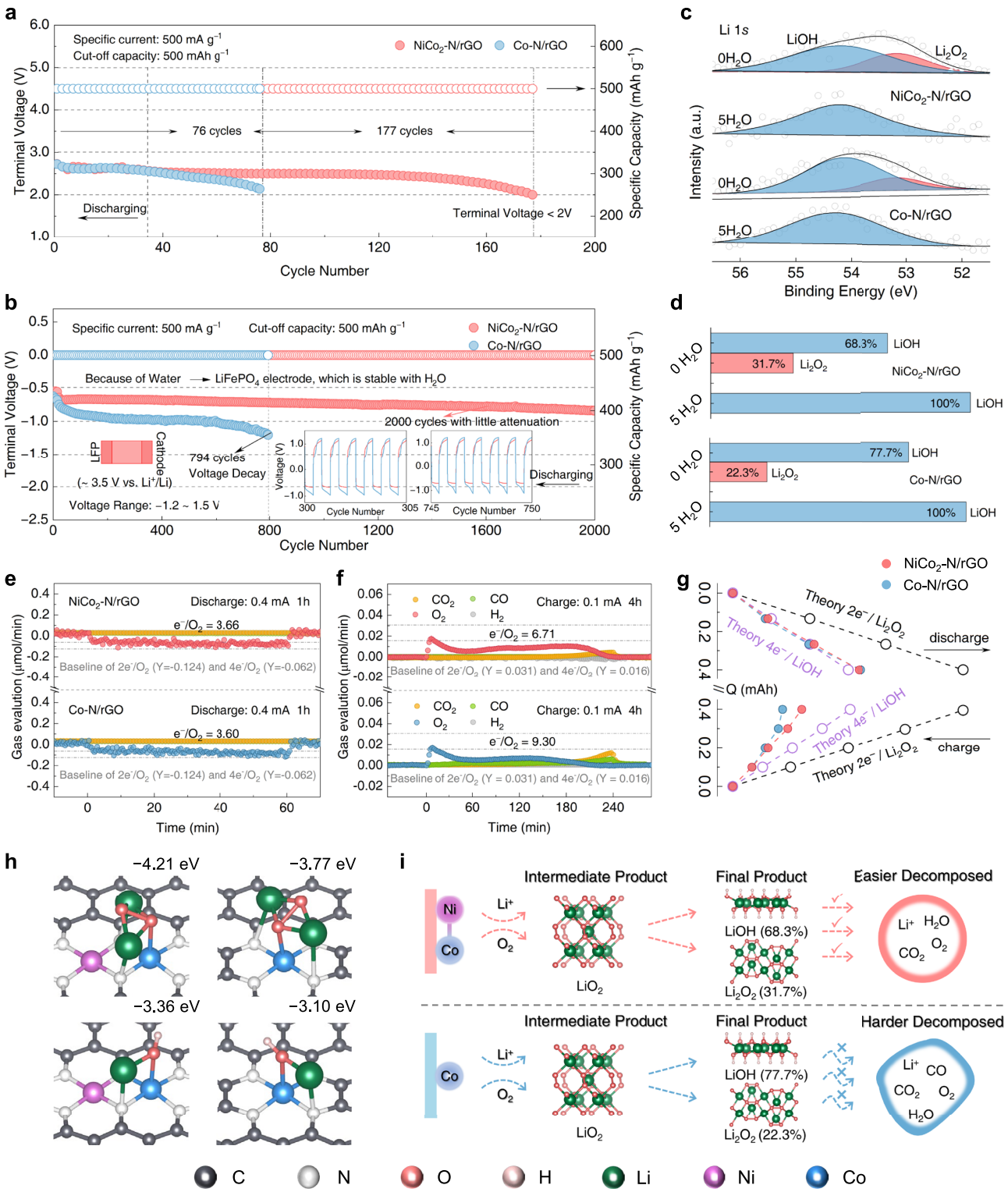

Fig. 5 | Analysis of cycling stability and catalytic process. Cycling performance of $NiCo_2$-DACs and Co-SACs electrodes in 2032-type coin cells at 500 mA g^{-1} with a capacity limit of 500 mA h g^{-1} in the electrolytes with **a** 0 vol% H_2O and **b** 5 vol% H_2O, respectively. The X-ray photoelectron spectroscopy (XPS) (**c**) and relative content (**d**) of the fully discharged (1st) product for $NiCo_2$-DACs and Co-SACs electrodes obtained at a specific current of 500 mA g^{-1} in the electrolytes with 0 vol % and 5 vol% H_2O, respectively. All cut-off capacities and specific currents mentioned above were normalized to the catalyst mass. Differential electrochemical mass spectrometry (DEMS) profiles with **e** discharge curves at 0.4 mA and **f** charge curves at 0.1 mA to a capacity of 0.4 mA h for the above two electrodes, with **g** overall analysis. The above electrochemical measurements were performed at 25 °C. **h** Adsorption energies of Li_2O_2 and LiOH on NiCo-DACs and Co-SACs, respectively. **i** Schematic illustration of the reaction process on $NiCo_2$-DACs and Co-SACs electrodes. Source data are provided as a Source Data file.

https://doi.org/10.1038/s41467-026-79335-6

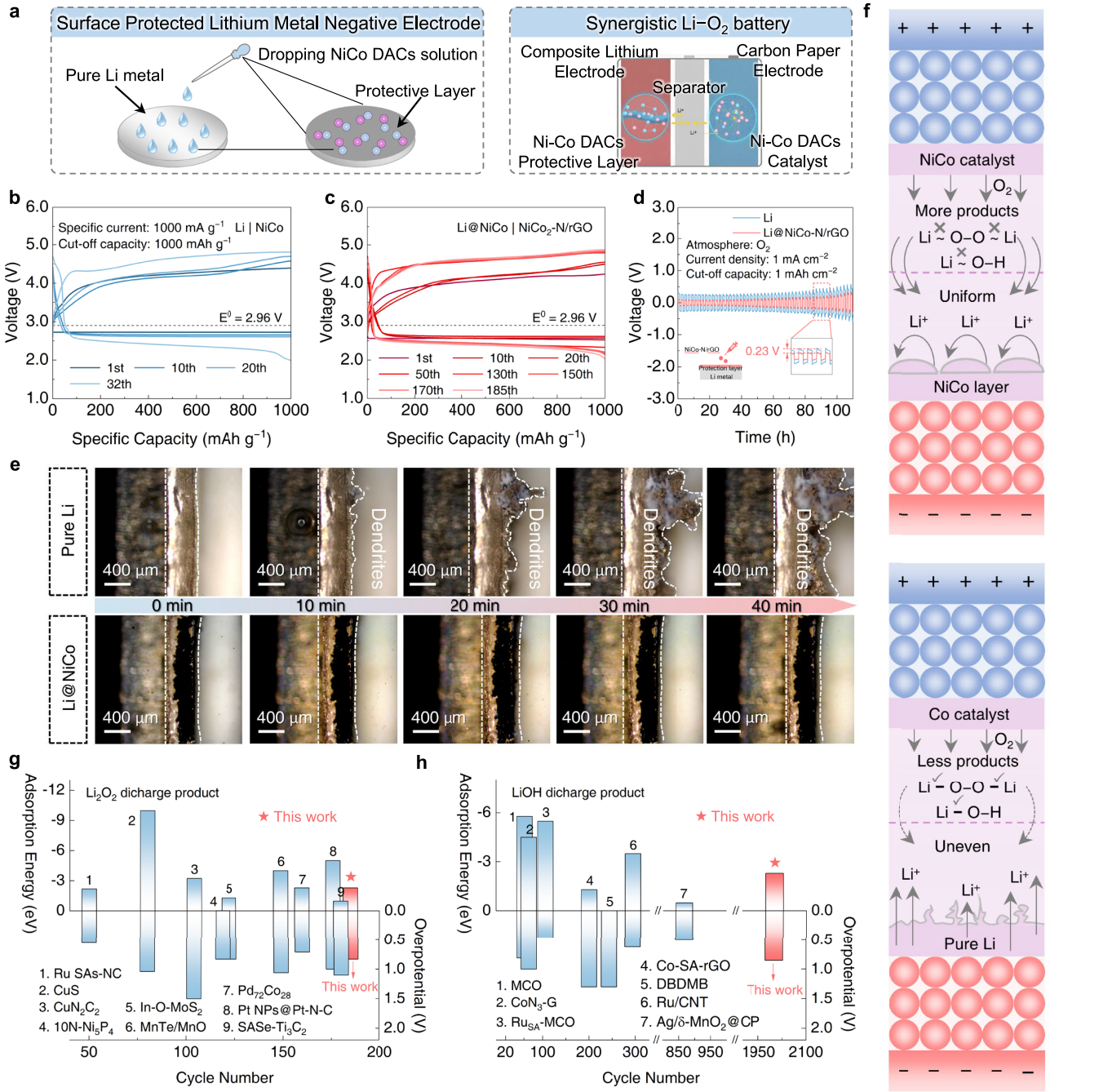

Fig. 6 | The role of a lithium composite metal negative electrode composed of NiCo dual-atom catalysts. a The preparation process of the lithium composite metal negative electrode and the structure of synergistic effect Li–O_2 batteries. **b**, **c** Galvanostatic discharge-charge profiles with $NiCo_2$-DACs as the positive electrode and pure lithium or lithium composite metal as the negative electrode at a limited capacity of 1000 mA h g^{-1} and a specific current of 1000 mA g^{-1} in the electrolyte with 0 vol% H_2O. All cut-off capacities and specific currents mentioned above were normalized to the catalyst mass. **d** Li plating/stripping behavior of symmetric batteries with the above two electrodes. The above electrochemical measurements were performed using 2032-type coin cells at 25 °C. **e** In situ optical microscopic observation of the Li plating process on pure lithium and lithium composite metal at 0.5 mA cm^{-2} under 25 °C. **f** Schematic diagram of mechanism summary. **g**, **h** Performance comparison toward overpotential, cycle number and intermediate product adsorption energy between Li–O_2 batteries with other reported catalysts (the underlying numerical values were summarized in Tables S4 and S5)[5,21,23–35]. Source data are provided as a Source Data file.

center to lower thermodynamic barriers for oxygen redox, while the dual-atom architecture simultaneously functions as a bifunctional stabilizer to homogenize Li^+ flux and suppress negative electrode dendrite growth. Broadly, this work provides a general strategy for the rational design of complex catalytic materials, offering a predictive strategy that can be readily extended to other multi-electron energy conversion processes beyond lithium–oxygen batteries.

Methods

Material synthesis

The original materials are graphite oxide aqueous solution (2 mg/mL, Suzhou TanFeng), nickel (II) chloride hexahydrate (≥99.9%, Aladdin), and cobalt (II) chloride hexahydrate (≥99.99%, Aladdin). In the synthesis process, firstly, 100 mg $NiCl_2{\cdot}6H_2O$ or $CoCl_2{\cdot}6H_2O$ was dissolving in 100 ml deionized water under vigorous agitation to prepare a stable precursor solution, respectively, corresponding to

https://doi.org/10.1038/s41467-026-79335-6

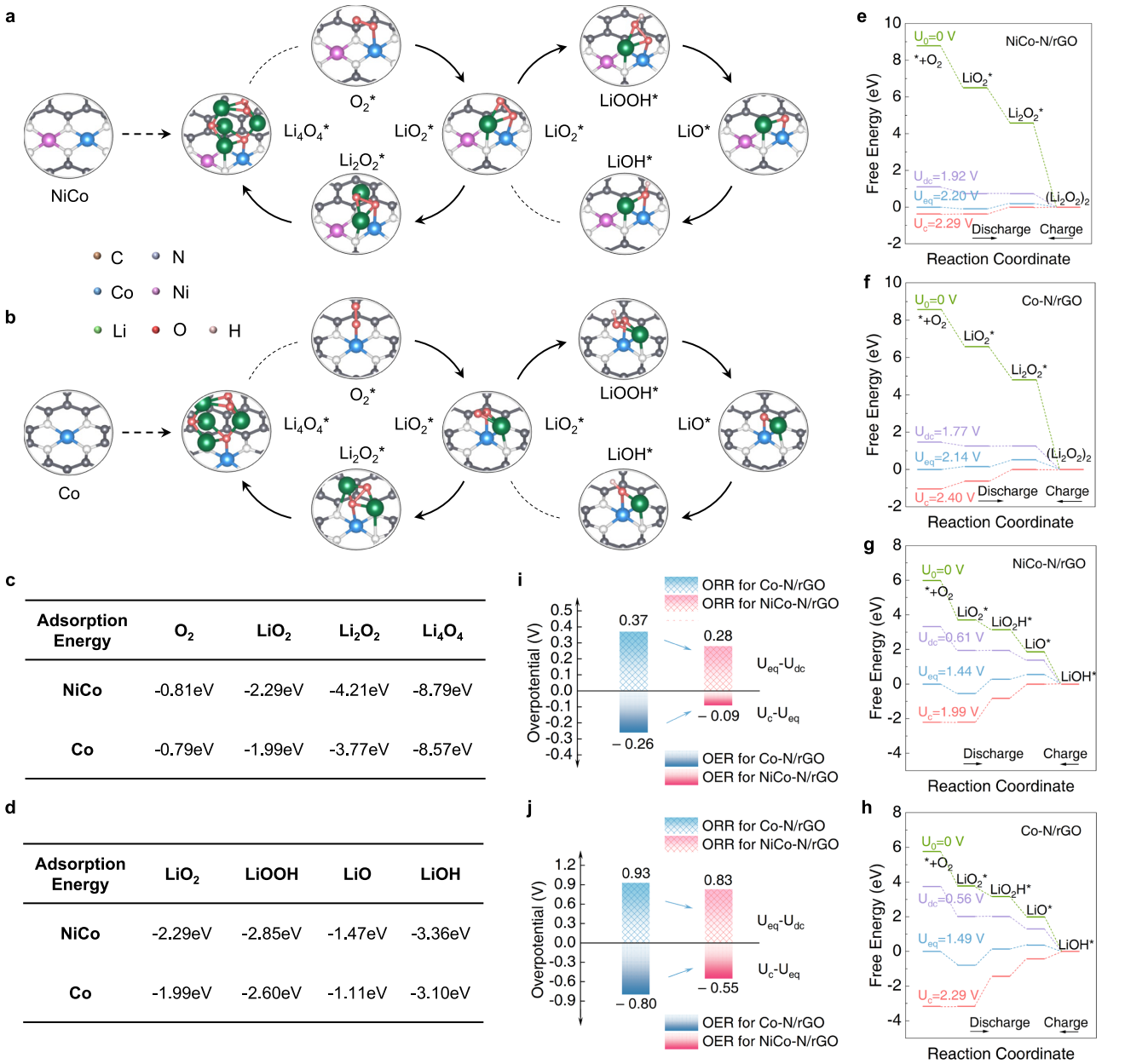

c

Adsorption Energy	O_2	LiO_2	Li_2O_2	Li_4O_4
NiCo	-0.81eV	-2.29eV	-4.21eV	-8.79eV
Co	-0.79eV	-1.99eV	-3.77eV	-8.57eV

d

Adsorption Energy	LiO_2	LiOOH	LiO	LiOH
NiCo	-2.29eV	-2.85eV	-1.47eV	-3.36eV
Co	-1.99eV	-2.60eV	-1.11eV	-3.10eV

Fig. 7 | Density functional theory (DFT) calculation simulation analysis using a k-point mesh of 1 × 1 × 1. a, **b** Generate reaction pathways for Li_2O_2 and LiOH on $NiCo_2$-DACs and Co-SACs electrodes, respectively (the brown, white, blue, purple, green, red, and pink spheres represent C, N, Co, Ni, Li, O, and H atoms). The optimized atomic configurations used for the Co-SAC and NiCo-DAC calculations were provided in Supplementary Data 1–4. **c**, **d** Adsorption energies of oxygen-containing species on above two electrodes. **e**–**h** Calculated free energy diagrams for the discharge-charge reactions on the above two electrodes. **i**, **j** The over-potential calculated by U_{eq} (equilibrium potential), U_{dc} (discharge potential), and U_c (charge potential). Source data are provided as a Source Data file.

concentrations of approximately 4.20 mmol L^{-1}. Afterward, different amounts of the above nickel salt solution and cobalt salt solution (for $NiCo_1$-N/rGO, $NiCo_2$-N/rGO, and $NiCo_3$-N/rGO, 25/50 µL, 100/50 µL, 200/50 µL of the Co/Ni precursor solutions, respectively) were transferred into 50 ml of GO solution to obtain a uniform mixture after 3 h of magnetic stirring and ultrasonic dispersion. Then, the black gel-like substances were achieved after hydrothermal treatment (100 mL Teflon-lined stainless-steel autoclaves) and three times cleaning by deionized water (100 mL per wash). It is noteworthy that the hydrothermal temperature was controlled at 180 °C and maintained for 6 h. Meanwhile, the collected samples were further freeze-dried for 72 h to remove the moisture inside. After that, the prepared materials underwent a simple annealing at 900 °C for 1 h in a tube furnace for high-temperature thermal reduction. The atmosphere was a streaming Ar (75 sccm)/NH_3 (25 sccm) mixture gas (100 ml min^{-1}) with a ramp rate of 5 °C min^{-1}. Finally, double metals containing catalytic materials NiCo-DACs, such as $NiCo_1$-N/rGO, $NiCo_2$-N/rGO, and $NiCo_3$-N/rGO were obtained (the content ratios of Co and Ni precursors are 0.5:1, 2:1, 4:1, respectively, and the final Co/Ni weight ratios determined by ICP-OES were ~0.6, ~2.4, and ~4.8 for $NiCo_1$-N/rGO, $NiCo_2$-N/rGO and $NiCo_3$-N/rGO, respectively), with two comparison groups (Ni-N/rGO and Co-N/rGO) being synthetized under the same conditions.

Electrode preparation

For the positive electrode, Ketjen Black (KB, EC-300J, Canrd Technology Co. Ltd.) and Polytetrafluoroethylene (PTFE, MA-EN-BI-0010, Canrd Technology Co. Ltd.) were used as the conductive agent and

binder, respectively. The weight ratio among the prepared catalytic materials, KB and PTFE, was 6:3:1. After mixing and grinding the above mixture evenly, a certain amount of dispersant isopropanol (≥99.5%, Macklin) was added to obtain a uniform and stable slurry, which would suffer stirring and ultrasonic. In addition, the carbon paper (CP, TGP-H-060, Canrd Technology Co. Ltd.) was tailored into circular discs with a diameter of 12 mm as the gas diffusion layer (GDL) in Li-O_2 batteries (LOBs), drying and cleaning them before used. Afterward, 100 μL slurry was slowly dropped onto the surface of CP, with pre-heating under 60 °C for 30 min, then vacuum drying at 90 °C for 12 h to finally obtain the catalytic positive electrode. The mass loading of NiCo-DACs (Ni/Co-SACs) was ca. 0.6 mg cm^{-2}. The specific capacity and current values were all normalized to the loading of catalyst (NiCo-DACs or Ni/Co-SACs). For the negative electrode, 3 mg NiCo-DACs were dispersed in 1 mL DME (≥99.5%, Aladdin) by stirring at 400 rpm for 3 h and sonication for 3 h, without the addition of binder. Lithium foil was cut into 16-mm-diameter discs using a cutting machine inside an Ar-filled glovebox (H_2O and O_2 < 1 ppm). Subsequently, 50 μL of the NiCo-DACs dispersion was uniformly drop-cast onto each Li disc and dried at 90 °C for 3 h in the Ar-filled glovebox to obtain the NiCo-coated lithium negative electrode.

Cell assembly and electrochemical measurements

The Li-O_2 cell was constructed in a 2032-type coin cell (stainless steel). All of the cells were assembled inside an Ar glove box (both H_2O content and O_2 content below 1 ppm) with a lithium foil electrode (≥99.99%, 300 μm in thick, and 16 mm in diameter, China Energy lithium Co., Ltd, which was cut into 16-mm-diameter discs using cutting machine inside an Ar-filled glovebox without additional surface cleaning) or the composite negative electrodes or $LiFePO_4$ electrode (LFP, MA-EN-CA-0015, Canrd Technology Co. Ltd.), a glass fiber separator (Whatman GF/D, MA-EN-SE-001209, thickness 675 μm, diameter 18 mm, pore size 2.7 μm, 2.6 s/100 mL/in^2, Canrd Technology Co. Ltd.), a catalytic oxygen electrode (NiCo-DACs, Ni/Co-SACs, 12 mm-diameter single-side, 0.2 mm in thick with an average mass of 10 mg. Before coating, the carbon paper was cleaned with alcohol and dried at 60 °C for 6 h) and 150 μL electrolyte containing 1 M LiTFSI in TEGDME (LK001, DoDoChem) with 0%/1%/3%/5% H_2O. Prior to measurements, all the cells were kept still at open circuits for the night in a hermetic container purged with desiccative ultra-pure O_2 (99.999%, 1.0 atm). Then, the electrochemical tests were performed in a galvanostatic mode employing a CT2001A LAND battery tester. For capacity-limited cycling tests, the voltage window depended on the negative electrode used. Cells employing Li metal or Li@NiCo as the negative electrode were cycled between 2.0 and 5.0 V, whereas cells employing $LiFePO_4$ (LFP) as the negative electrode were cycled between −1.2 and 1.5 V. The electrochemical impedance spectroscopy of the cell was evaluated using a CHI660E electrochemical workstation (Shanghai Chenhua Instrument Co., Ltd.) in potentiostatic mode over a frequency range of 0.01–10^5 Hz with an amplitude of 10 mV (6 points per decade). Before each measurement, the cell was equilibrated at open-circuit voltage for 6 h. EIS measurements were conducted at 25 °C under the cell states and electrolyte conditions specified in the corresponding figure captions. CV tests were conducted on the same workstation within 2.0–4.5 V at a scan rate of 0.1 mV s^{-1}. All the electrochemical measurements were implemented in a Neware battery cycler (CT-4008) in a climate chamber at 25 °C.

Characterizations

The morphology of the as-prepared catalysts (NiCo-DACs, Ni/Co-SACs) and the electrochemical reaction products was examined by field-emission scanning electron microscopy (FESEM; Hitachi SU8010) equipped with energy-dispersive X-ray spectroscopy and a vacuum-transfer system. Transmission electron microscopy (TEM) measurements were performed using a Tecnai G2 Spirit operated at 120 kV, while high-resolution TEM images were obtained using an FEI Tecnai G2 F30. Atomic-scale structural features were further examined by high-angle annular dark-field scanning transmission electron microscopy (HAADF-STEM) using a probe-corrected transmission electron microscope equipped with spherical-aberration correctors. For electron microscopy measurements, powder samples were ultrasonically dispersed in ethanol (water content ≤0.2%, Aladdin) before specimen preparation. Nitrogen adsorption/desorption measurements were carried out using an ASAP2020M+C analyzer to determine the specific surface area and pore-size distribution. Powder X-ray diffraction (XRD) patterns were collected on a Rigaku D/Max 2500 diffractometer using Cu Kα radiation (λ = 1.5406 Å) at 36 kV and 25 mA. For ex situ analysis of discharged or recharged positive electrodes, the washed electrodes were protected from ambient moisture and CO_2 during sample preparation and transfer. Raman spectra were recorded at room temperature using a Renishaw inVia confocal Raman spectrometer with a 532 nm excitation laser. Mica substrates were used for Raman measurements of electrodes recovered after discharge or charge. Surface elemental compositions and chemical states were characterized by X-ray photoelectron spectroscopy (XPS; PHI 5000 VersaProbe II), with binding energies referenced to the C 1*s* signal at 284.8 eV. The Ni and Co contents of the catalysts were quantified by inductively coupled plasma optical emission spectroscopy (ICP-OES; Varian 720-ES) after acid digestion. The atomic and electronic structures were evaluated via Co/Ni K-edge XAFS measurements in fluorescence mode at 25 °C under air conditions. Co/Ni foil and CoO/Co_3O_4/NiO for the Co/Ni K-edge was used to calibrate energy. The powder samples were pressed into pellets and sealed between Kapton films. The obtained XAFS data was processed in Athena (version 0.9.26) for background, pre-edge line, and post-edge line calibrations. Then Fourier transformed fitting was carried out in Artemis (version 0.9.26). The k^3 weighting, *k*-range of 3–~12.5 $Å^{-1}$, and *R* range of 1–3 Å were used for the fitting of Co foil. The k^3 weighting, *k*-range of 3–~15 $Å^{-1}$ and *R* range of 1–3 Å were used for the fitting of Ni foil. The k^3 weighting, *k*-range of 3–~10 $Å^{-1}$, and *R* range of 1–2 Å were used for the fitting of samples. The four parameters, coordination number, bond length, Debye-Waller factor and E_0 shift (CN, R, and ΔE_0) were fitted without anyone was fixed, the σ^2 was set. For Wavelet Transform analysis, the $\chi(k)$ exported from Athena was imported into the Hama Fortran code. The parameters were listed as follows: *R* range, 0–4 Å; *k* range, 0–16 $Å^{-1}$; k weight, 2; and the Morlet function with κ = 10, σ = 1 was used as the mother wavelet to provide the overall distribution. The kinetic isotope effect (KIE) performance was evaluated by using a standard three-electrode system on a CHI 660E electrochemical workstation (Shanghai Chenhua, China) in freshly prepared 0.1 M KOH (in H_2O, Aladdin) and 0.1 M KOD (in D_2O, ≥99.9 atom% D, Aladdin) electrolyte. In situ differential electrochemical mass spectrometry (DEMS) was performed using a QAS 100Li system coupled to a custom gas-flow Li-O_2 cell (Supplementary Fig. 48). The cell consisted of a 15-mm-diameter catalytic air electrode, a GF/D glass-fiber separator, a Li-metal negative electrode, a stainless-steel mesh, a spring and a PTFE sleeve. The cell contained 30 μL electrolyte and was operated at 25 °C under O_2/Ar flow at 1/0.09 mL min^{-1} and 0/12.6 mL min^{-1} for discharge and charge process, respectively, under atmospheric pressure. Before electrochemical testing, the gas flow was maintained for 6 h to establish a stable mass-spectrometric baseline. The cell was discharged galvanostatically at 0.4 mA to 0.4 mA h and subsequently charged at 0.1 mA. Signals at m/z = 2, 28, 32 and 44, corresponding to H_2, CO, O_2, and CO_2, respectively, were monitored using QAS 100 Li supporting device. The total amount of each gas was obtained by integrating the calibrated molar-flow rate over time. The electron-to-oxygen ratio was calculated as $n_e^-/n_{O2} = Q/(Fn_{O2})$, where *Q* is the integrated electrochemical charge, *F* is the Faraday constant, and n_{O2} is the amount of O_2 consumed during discharge or evolved during charge. The acid-base titration using 0.1 M HCl (Aladdin) and

phenolphthalein (0.5%, Aladdin) was employed to quantitatively characterize the discharge products. The harvested positive electrodes and separators were immediately immersed in 5.0 mL of ultrapure H_2O without washing or drying and vigorously shaken for 20 s to dissolve the LiOH discharge products. The resulting solution was titrated with 0.1 M HCl standardized using a Na_2CO_3 standard solution, with 0.05 mL phenolphthalein in isopropanol used as the endpoint indicator. The electrolyte compositions were recorded using a Varian DD2 400 MHz spectrometer, and the NMR solvent is DMSO (≥99.9%, Aladdin). For ex situ XRD, XPS, SEM, NMR, and titration characterizations, cells were disassembled in an Ar-filled glovebox at the electrochemical states specified in the corresponding figure captions. The harvested electrodes were washed three times with DME to remove residual electrolyte and soluble salts, and then dried in the glovebox. The samples were subsequently sealed or transferred under an inert/vacuum environment to minimize exposure to moisture and CO_2 before measurement. The electrolytes were harvested and extracted with DMSO, and the resulting solutions were sealed in NMR tubes before transfer for measurement. Sample harvesting and transfer were conducted at 25 °C, and the interval between cell disassembly and sample sealing/measurement was within 1 h. In situ optical microscopy was performed using a custom-built transparent electrochemical cell, and two identical pure Li or Li@NiCo electrodes were used as the working electrode, with 10 μL electrolyte containing 1 M LiTFSI in TEGDME (LK001, DoDoChem). The Li plating process was monitored using an optical microscope (Yuescope, China) at a current density of 0.5 mA cm^{-2} under 25 °C. Optical images were recorded at 0, 10, 20, 30, and 40 min under identical acquisition conditions.

Computational details

The DS-PAW (version: 2023A) package was used to perform the density functional theory (DFT) calculations. The Perdew–Burke–Ernzerhof (PBE) functional within the generalized gradient approximation (GGA) was used to describe the exchange-correlation functional. The core-valence electron interaction was represented by the project-augmented wave (PAW) method (https://hzwtech.com/Device%20Studio/DS-PAW/build/html/ppfile.html), and the cutoff energy of plane-wave basis was set to 450 eV. The DFT-D3 method was used to describe dispersion interactions. The graphene matrix was modeled with a 7 × 7 supercell and a vacuum of 15 Å with the Device Studio software (version: 2023A). For vacuum calculations, no dielectric or explicit-solvent correction was included. A k-points mesh of 1 × 1 × 1 and 2 × 2 × 1 was used in the optimization (Supplementary Data 1–4). During the structural optimization, all atoms in the model were completely relaxed. The electronic self-consistent-field calculations were converged to (10^{-5}) eV. Occupations were treated using Gaussian smearing with a width of 0.05 eV, and the reported total energies were extrapolated to zero smearing. During geometry optimization, the lattice vectors were fixed, whereas all atoms were allowed to relax without symmetry constraints. A dipole correction was not applied. The geometry optimization is stopped as the maximal force on each relaxed atom was less than 0.05 eV/Å. All calculations were spin-polarized, and the magnetic moments were automatically initialized and optimized self-consistently during the electronic-structure calculations. The adsorption energy (E_{ads}) was calculated according to the following equation: $E_{ads} = E_{X/surf} - E_{surf} - E_X$, where $E_{X/surf}$, E_{surf}, and E_X are the energies of the substrate with adsorbate, the substrate, and the adsorbate molecule. The Gibbs free-energy change of each elementary step at temperature (T = 300 K) was obtained from $\Delta G = \Delta E + \Delta E_{ZPE} + T\Delta S$, where ΔE is the total energy difference from DFT, ΔE_{ZPE} is the zero-point energy correction, and $T\Delta S$ is the entropy contribution. Vibrational frequencies were used to calculate the zero-point energy and entropy contributions. The vibrational enthalpy and entropy of adsorbed species were evaluated within the harmonic approximation. For the overestimation of the binding energy of the O-O bond in O_2 using the standard GGA approximation, here we used the corrected O_2 energy, which can be calculated according to the experimental formation energy of Li_2O_2 from Li metal and O_2 gas. For $2Li(s) + O_2(g) \rightarrow Li_2O_2(s)$, the experimental equilibrium potential is 2.96 V, corresponding to a reaction free energy of ($\Delta G = -5.92$ eV) per Li_2O_2 formula unit. The calculated Li_2O_2 unit cell contains two formula units, whereas the calculated Li unit cell contains two Li atoms. Therefore, the corrected O_2 energy was obtained as E_{Li2O2}-$2E_{Li}$-ΔG, where E_{Li2O2} and E_{Li} are equal to −19.05 eV, −2.00 eV, respectively, from DS-PAW. The corrected O_2 energy was used consistently in all subsequent reaction energy calculations involving O_2. The optimized atomic configurations used for the DFT calculations are provided in Supplementary Data 1–4. The d-band center was calculated as the first moment of the projected d-state density of states:

$$\varepsilon_d = \frac{\int_{E_{min}}^{E_{Max}} E D_d(E) dE}{\int_{E_{min}}^{E_{Max}} D_d(E) dE}$$

where $D_d(E)$ represents the projected d state density of states, E is the energy relative to the Fermi level E_f = 0 eV, and the integration was performed over all occupied d states below the Fermi level. The work function was determined from the difference between the vacuum electrostatic potential and the Fermi energy:

$$\Phi = E_{vac} - E_F$$

where V_{vac} is the vacuum potential obtained from the plateau region of the plane-averaged electrostatic potential along the surface normal direction. Electron transfer was quantified using Bader charge analysis based on the self-consistent valence electron density. The electron-localization function was evaluated from the converged self-consistent electron density using the ELF implementation in DS-PAW.

Machine-learning method

To systematically navigate the vast chemical space and elucidate the complex structure-activity relationships (SARs) governing battery performance (including overpotential (Y_1) and cycling performance (Y_2)), we established an integrated and interpretable machine learning framework. Firstly, we assembled a dataset of 200 records covering the M_1-M_2-N catalyst configurations represented in the source data from publicly available literature reports. Records lacking an identifiable catalyst composition or a usable overpotential value were excluded, while multiple records from the same publication were retained when they represented distinct catalyst configurations or measurements. The corresponding source DOIs and extracted data are provided in the Data Availability section. Each record was described using nearly 50 atomic, electronic, and physical descriptors. Missing or non-numeric descriptor values were converted to zero before machine-learning analysis. Then, the elemental strings in the Compounds(M_1-M_2-N) column were parsed into the M_1 and M_2 positions and separately encoded using one-hot encoding, resulting in 18 M_1 indicators and 16 M_2 indicators (34 composition-encoding variables in total). To reduce source-dependent information leakage, the data source variable, representing the literature source of each record, was used as the grouping variable. The 151 source groups were randomly ordered using seed 42 and partitioned into five group-wise folds. Each group was assigned exclusively to either the training or held-out set within each fold. The five folds contained 160/40, 159/41, 163/37, 163/37, and 155/45 training/held-out records, corresponding to approximately 80/20 overall. Each record served as a held-out observation once, and no separate validation or independent final test set was used. Hyperparameter optimization and performance evaluation were conducted using these same five group-wise folds.

Recognizing the intrinsic complexity of catalytic origins, we benchmarked an ensemble of eight distinct regression algorithms to capture high-dimensional data patterns. These included linear models (Ridge, Lasso, ElasticNet, and SVM) and non-linear ensemble methods (Random Forest, ExtraTrees, XGBoost, and Gradient Boosting). Each model was optimized by exhaustive grid search using the mean coefficient of determination (R^2) across the five group-wise cross-validation folds as the selection criterion. The same five group-wise folds were used for hyperparameter selection and held-out performance evaluation. The search spaces and selected hyperparameters for all eight models are summarized in Table S7. The selected XGBoost configuration achieved the highest mean held-out-fold performance, with an R^2 of 0.8815 ± 0.0346. In addition, we also conducted 50 held-out folds in total with 10 random seeds on this model to avoid the randomness of this result, and it showed that the average R^2 of different random seeds was not less than 0.85, ensuring robust stability and predictive performance. To obtain interpretable physicochemical insights, we applied SHAP to the optimized XGBoost model and ranked the input variables according to their mean absolute SHAP values. The results indicate that intrinsic electronic properties are the dominant factors, particularly the correction of d electron number of the main metal site (M_1) with the electronegativity of the non-metal site (N), the correction of d electron number of M_1 with the average electronegativity of the second metal site (M_2) and N, as well as the d-band center of M_1. Subsequently, we used the trained model to evaluate the elemental combinations represented by the 28 distinct element symbols in the dataset. Among the evaluated configurations, the Co–Ni heteronuclear pair exhibited the lowest mean predicted overpotential. Meanwhile, it is noteworthy that, the cycling performance (Y_2, final indicators of Li-O_2 batteries) will increase with the decrease of overpotential, identifying the Co–Ni heteronuclear pair as a better configuration. Detailed reproducibility of the dataset, five-fold group-wise cross-validation, model implementation seeds, software versions, and SHAP analysis procedure is described in Supplementary Note 1.

Data availability

The data used in this study have been deposited in the Zenodo repository (https://doi.org/10.5281/zenodo.22731985). Source data are provided with this paper.

Code availability

The machine-learning code used in this study is publicly available at https://github.com/JohnResse1/ML_code_four-electron-LiOH-pathway-for-ultra-stable-lithium-oxygen-batteries. A permanent and citable snapshot of the version used in this study has been archived in Zenodo[22] and is available under the https://doi.org/10.5281/zenodo.22731985.

References

1. Zhang, J. Q. et al. A long-life lithium-oxygen battery via a molecular quenching/mediating mechanism. *Sci. Adv.* **8**, eabm1899 (2022).
2. Kim, M. et al. Carbon-free high-performance cathode for solid-state Li-O_2 battery. *Sci. Adv.* **8**, eabm8584 (2022).
3. Ke, S. W. et al. Covalent organic frameworks with Ni-Bis(dithiolene) and Co-porphyrin units as bifunctional catalysts for Li-O_2 batteries. *Sci. Adv.* **9**, eadf2398 (2023).
4. Bai, T. S. et al. Recent progress on single-atom catalysts for lithium-air battery applications. *Energy. Environ. Sci.* **16**, 1431–1465 (2023).
5. Wang, P. et al. P-block element modulated 1 T phase MoS_2 with Ru lattice grafting for high-performance Li||O_2 batteries. *Nat. Commun.* **16**, 1453 (2025).
6. Wang, J. et al. Lithium nitrate-mediated low-volatile deep eutectic electrolyte for highly stable lithium-oxygen batteries. *ACS Nano* **19**, 11284–11294 (2025).
7. Liu, T. et al. Cycling Li-O_2 batteries via LiOH formation and decomposition. *Science* **350**, 530–533 (2015).
8. Wang, G. et al. Toward practical photo-assisted Li-O_2 batteries: a four-electron pathway enabled by Ru-doped β-MnO_2. *Adv. Mater.* **37**, 2507891 (2025).
9. Song, L. N. et al. Dual active intermediates induced LiOH formation via the OH-rich proton donor in Li-O_2 batteries. *Adv. Funct. Mater.* **35**, 2414854 (2025).
10. Lu, J. et al. Co_3O_4-catalyzed LiOH chemistry in Li-O_2 batteries. *ACS Energy Lett.* **5**, 3681–3691 (2020).
11. Lu, J. et al. A lithium–oxygen battery based on lithium superoxide. *Nature* **529**, 377–382 (2016).
12. Xia, C., Kwok, C. Y. & Nazar, L. F. A high-energy-density lithium-oxygen battery based on a reversible four-electron conversion to lithium oxide. *Science* **361**, 777–781 (2018).
13. Kondori, A. et al. A room temperature rechargeable Li_2O-based lithium-air battery enabled by a solid electrolyte. *Science* **379**, 499–505 (2023).
14. Bai, T. et al. Modulating electronic environment and coordination structure of ruthenium with ultralow loading atomic nickel toward highly reversible Li-O_2 batteries. *Adv. Funct. Mater.* **35**, 2424014 (2025).
15. Bai, T. et al. Atomic Ni-catalyzed cathode and stabilized Li metal anode for high-performance Li–O_2 batteries. *eScience* **5**, 100310 (2025).
16. Han, Z. et al. Machine learning-based design of electrocatalytic materials towards high-energy lithium||sulfur batteries development. *Nat. Commun.* **15**, 8433 (2024).
17. Chen, S. et al. External Li supply reshapes Li deficiency and lifetime limit of batteries. *Nature* **638**, 676–683 (2025).
18. Sun, J. et al. Artificial-intelligence-guided design of ordered gas diffusion layers for high-performing fuel cells via Bayesian machine learning. *Nat. Commun.* **16**, 6528 (2025).
19. Lao, Z. et al. Data-driven exploration of weak coordination microenvironment in solid-state electrolyte for safe and energy-dense batteries. *Nat. Commun.* **16**, 1075 (2025).
20. Sun, C. et al. Partial-oxidation enabling homologous Ru/RuO_2 heterostructures with proper *d*-band center as efficient and durable cathode catalysts for ultralong cycle life in Li–O_2 batteries. *Adv. Energy Mater.* **15**, 2402699 (2025).
21. Yin, S. et al. Engineering of MnTe/MnO heterostructures with interfacial electric field modulation for efficient and durable Li–O_2 batteries. *Small* **20**, 2406525 (2024).
22. Bai, T. & Hu, Y. et al. Data and code for "Machine learning-driven regulation of the four-electron LiOH pathway in lithium–oxygen batteries with prolonged cycling". https://doi.org/10.5281/zenodo.22731985 (2026).
23. Feng, J. et al. Defect engineering in CuS_{1-x} nanoflowers enables low-overpotential and long-cycle-life of lithium-oxygen batteries. *Small* **20**, 2406081 (2024).
24. Hu, X. et al. Ru single atoms on N-doped carbon by spatial confinement and ionic substitution strategies for high-performance Li–O_2 batteries. *J. Am. Chem. Soc.* **142**, 16776–16786 (2020).
25. Huang, K. et al. Cobalt single atom-catalyzed formation of LiOH in Li-O_2 batteries via the direct 4-electron oxygen reduction pathway. *CCS Chem.* **6**, 2502–2514 (2024).
26. Zhang, W. et al. Water-trapping single-atom Co-N_4/graphene triggering direct 4e^- LiOH chemistry for rechargeable aprotic Li–O_2 batteries. *Small* **19**, 2301391 (2023).
27. Xiong, Q., Huang, G. & Zhang, X.-B. High-capacity and stable Li-O_2 batteries enabled by a trifunctional soluble redox mediator. *Angew. Chem. Int. Ed.* **59**, 19311–19319 (2020).
28. Zhang, X. et al. Unravelling the complex LiOH-based cathode chemistry in lithium–oxygen batteries. *Angew. Chem. Int. Ed.* **62**, e202212942 (2023).

29. Dai, L. et al. Reversible LiOH chemistry in Li-O_2 batteries with free-standing Ag/δ-MnO_2 nanoflower cathode. *Sci. China Mater.* **65**, 1431–1442 (2022).
30. Li, X. et al. Tailoring lithium-peroxide reaction kinetics with CuN_2C_2 single-atom moieties for lithium-oxygen batteries. *Nano Energy* **93**, 106810 (2022).
31. Han, X., Zhao, L., Wang, J., Liang, Y. & Zhang, J. Delocalized electronic engineering of Ni_5P_4 nanoroses for durable Li-O_2 batteries. *Adv. Mater.* **35**, 2301897 (2023).
32. Zhou, Y. et al. D-orbital reconstruction achieves low charge overpotential in Li-oxygen batteries. *Nat. Commun.* **16**, 3353 (2025).
33. Guo, Y. et al. Dual-type atomic Ru promoted bifunctional catalytic process realizing ultralow overpotential for Li-O_2 batteries. *Appl. Catal. B Environ.* **356**, 124203 (2024).
34. Zhao, D. et al. Single semi-metallic selenium atoms on Ti_3C_2 MXene nanosheets as excellent cathode for lithium–oxygen batteries. *Adv. Funct. Mater.* **31**, 2010544 (2021).
35. Zhao, S.-Z. et al. Asymmetric catalytic site driving LiOH chemistry for Li-O_2 batteries based on cationic vacancy-derived single-atom spinel. *ACS Catal.* **14**, 7332–7344 (2024).

Acknowledgements

We thank the Analysis and Testing Center at Harbin Institute of Technology, Shenzhen, for the material characterizations.

Author contributions

L.C. and D.L. conceived the concept and supervised the overall project. T.B., Y.H., W.Z., and X.Z. contributed equally to this work. T.B. and Y.H. performed the material synthesis, characterizations, and electrochemical measurements. W.Z. and X.Z. conducted the machine learning modeling and density functional theory (DFT) calculations. J.H., J.W., W.S., T.R., and S.D. assisted with data collection and analysis. D.G., J.L., and R.S. provided theoretical guidance and participated in the discussion of results. T.B. wrote the original draft. L.C., D.L., D.G., J.L., and R.S. reviewed and revised the manuscript. All authors discussed the results and approved the final submission.

Funding

D.G., J.L., R.S., L.C., and D.L. disclose support for the research of this work from New Generation Artificial Intelligence-National Science and Technology Major Project (2026ZD0127803), National Natural Science Foundation of China (Grant Nos. 52672046, 52002094; 22479037; 52571006), Advanced Materials-National Science and Technology Major Project (Grant Nos. 2025ZD0618801; 2026ZD0127800), Guangdong Basic and Applied Basic Research Foundation (Grant No. 2025A1515011995), Shenzhen Science and Technology Program (Grant Nos. SGCX20250526152800001; GXWD20221030205923001; SYSPG20241211173609003), Shenzhen Basic Research Project (Natural Science Foundation: JCYJ20241202123504007), State Key Laboratory of Precision Welding & Joining of Materials and Structures (Grant No. 24-Z-17, 24-T-08), the Fundamental Research Funds for the Central Universities (MSE.'AI+CL'JZPY.2026006; HIT.DZJJ.2026058).

Competing interests

The authors declare no competing interests.

Additional information

Supplementary information The online version contains Supplementary Material available at https://doi.org/10.1038/s41467-026-79335-6.

Correspondence and requests for materials should be addressed to Dandan Gao, Jingyu Lu, Rongpei Shi, Lijie Ci or Deping Li.

Peer review information *Nature Communications* thanks the anonymous reviewer(s) for their contribution to the peer review of this work. A peer review file is available.

Reprints and permissions information is available at http://www.nature.com/reprints

Publisher's note Springer Nature remains neutral with regard to jurisdictional claims in published maps and institutional affiliations.

Open Access This article is licensed under a Creative Commons Attribution 4.0 International License, which permits use, sharing, adaptation, distribution and reproduction in any medium or format, as long as you give appropriate credit to the original author(s) and the source, provide a link to the Creative Commons licence, and indicate if changes were made. The images or other third party material in this article are included in the article's Creative Commons licence, unless indicated otherwise in a credit line to the material. If material is not included in the article's Creative Commons licence and your intended use is not permitted by statutory regulation or exceeds the permitted use, you will need to obtain permission directly from the copyright holder. To view a copy of this licence, visit http://creativecommons.org/licenses/by/4.0/.

© The Author(s) 2026

[1]State Key Laboratory of Precision Welding & Joining of Materials and Structures, School of Materials Science and Engineering, Harbin Institute of Technology (Shenzhen), Shenzhen, China. [2]Department of Chemistry, City University of Hong Kong, Hong Kong, China. [3]College of Chemistry and Environmental Engineering, Shenzhen University, Shenzhen, China. [4]School of Science, Harbin Institute of Technology (Shenzhen), Shenzhen, China. [5]Department of Chemistry, Johannes Gutenberg University, Mainz, Mainz, Germany. [6]Shenzhen Key Laboratory of New Materials Technology, Shenzhen, China. [7]These authors contributed equally: Tiansheng Bai, Yiming Hu, Wei Zhai, Xiongwei Zhong. ✉e-mail: dandan.gao@uni-mainz.de; lujingyu@hit.edu.cn; shirongpei@hit.edu.cn; cilijie@hit.edu.cn; lideping@hit.edu.cn